npj | computational materials

Article

Published in partnership with the Shanghai Institute of Ceramics of the Chinese Academy of Sciences

https://doi.org/10.1038/s41524-024-01434-z

Enhanced spin Hall ratio in two-dimensional semiconductors

Jiaqi Zhou [1] ✉, Samuel Poncé [2,3] ✉ & Jean-Christophe Charlier [1] ✉

The conversion efficiency from charge current to spin current via the spin Hall effect is evaluated by the spin Hall ratio (SHR). Through state-of-the-art ab initio calculations involving both charge conductivity and spin Hall conductivity, we report the SHRs of the III-V monolayer family, revealing an ultrahigh ratio of 0.58 in the hole-doped GaAs monolayer. In order to find more promising 2D materials, a descriptor for high SHR is proposed and applied to a high-throughput database, which provides the fully relativistic band structures and Wannier Hamiltonians of 216 exfoliable monolayer semiconductors and has been released to the community. Among potential candidates for high SHR, the MXene monolayer Sc_2CCl_2 is identified with the proposed descriptor and confirmed by computation, demonstrating the descriptor validity for high SHR materials discovery.

The Hall effect encompasses a wide range of phenomena which realize the conversion between various physical properties[1,2]. The strength of the Hall effect can be denoted by $\beta = \tan(\theta_H) = E_H/E$ where θ_H is the Hall angle, E_H is the transverse Hall field, and E is the longitudinal electric field[3]. Correspondingly, the strength of the spin Hall effect (SHE) is given by the spin Hall ratio (SHR) as $\xi = \tan(\theta_{SH}) = \frac{2e}{\hbar}\left|\frac{J_s}{J_c}\right|$ where θ_{SH} is the spin Hall angle, J_s is the transverse spin Hall current density, and J_c is the longitudinal charge current density. SHR is often used as a proxy to indicate the charge-to-spin conversion efficiency, which is crucial for low-power-consumption spintronic applications[4–6]. Indeed, when θ_{SH} is small, the first-order Taylor polynomial gives $\xi \approx \theta_{SH}$, which is a good approximation for the bulk semiconductors and metals where $\xi \sim 0.01$[7–9]. Recently, enhanced SHR has been found in van der Waals materials with strong spin-orbit coupling (SOC). Huge SHRs over 10 are reported in topological insulators[10,11] while large SHR ~ 0.5 in $MoTe_2$ and WTe_2 Weyl semimetals have also been theoretically and experimentally identified[12–15]. However, the relative abundance of topological materials is around 1%[16,17], limiting material options for device manufacturing. The various two-dimensional (2D) materials enable a preferable compatibility with the integrated circuit[18] with desirable properties. For instance, the MoS_2 monolayer can exhibit $\xi = 0.14$ induced by the Rashba-Edelstein effect[19]. Note that large ξ will break the approximation $\xi \approx \theta_{SH}$, and therefore, the spin Hall ratio rather than the spin Hall angle should be used to denote the ratio of spin current to charge current. 2D materials composed of heavy atoms are promising for SHE[20,21] since the strong SOC can induce a large spin Hall conductivity (SHC), and doping is an effective way to manipulate the transport behaviors in semiconductors. Both factors can promote SHR enhancement in 2D semiconductors.

Although charge transport and SHC have been separately investigated in 2D materials[22–26], the study of SHR remains elusive due to the multidisciplinary complexity involving the electron-phonon interaction (EPI) for electron motion[27,28] and SOC for spin transport[4,5]. In the present work, we report the spin Hall ratios in monolayer semiconductors using density functional theory (DFT)[29], density functional perturbation theory (DFPT)[30], and Wannier functions[31]. The family of III-V monolayer semiconductors (MX, M=Ga, In, and X = As, Sb) are investigated. In the hole-doped regimes, the charge conductivities are significantly suppressed by the strong inter-peak scattering, while high SHCs occur due to the strong SOC, yielding an ultrahigh SHR of $\xi = 0.58$ in the GaAs monolayer. Taking the transport behaviors of III-V monolayers as a prototype, we propose a general descriptor for the high SHR based on the electronic structures. To validate the generality of this descriptor, we create a high-throughput database by performing fully relativistic DFT calculations and Wannierizations on 216 monolayer semiconductors, whose electronic band structures, effective masses, and SHCs have been calculated. The database is screened by the descriptor and suggests two MXene candidates, Sc_2CCl_2 and Y_2CBr_2 monolayers. The charge conductivities are investigated in both materials, confirming high SHR and validating the proposed SHR descriptor.

Results and discussions

Charge transport

The phonon-limited charge conductivity in a doped 2D semiconductor is calculated as[32]

$$\sigma_{\alpha\beta} = \frac{-e}{S^{uc}} \sum_n \int \frac{d^2\mathbf{k}}{\Omega^{BZ}} v_{n\mathbf{k}\alpha} \partial_{E_\beta} f_{n\mathbf{k}}, \quad (1)$$

[1]Institute of Condensed Matter and Nanosciences (IMCN), Université catholique de Louvain (UCLouvain), Chemin des Étoiles 8, B-1348 Louvain-la-Neuve, Belgium. [2]European Theoretical Spectroscopy Facility and Institute of Condensed Matter and Nanosciences (IMCN), Université catholique de Louvain (UCLouvain), Chemin des Étoiles 8, B-1348 Louvain-la-Neuve, Belgium. [3]WEL Research Institute, Avenue Pasteur 6, B-1300 Wavre, Belgium.
✉e-mail: jiaqi.zhou@uclouvain.be; samuel.ponce@uclouvain.be; jean-christophe.charlier@uclouvain.be

where α and β are Cartesian directions, S^{uc} is the unit cell area, Ω^{BZ} is the first Brillouin zone area, and $v_{n\mathbf{k}\alpha} = \hbar^{-1}\partial\varepsilon_{n\mathbf{k}}/\partial k_\alpha$ is the band velocity, n is the band index. The linear variation of the electronic occupation function $f_{n\mathbf{k}}$ in response to $\mathbf{E}$, $\partial_{E_\beta} f_{n\mathbf{k}}$, can be obtained by solving the Boltzmann transport equation given by Supplementary Equation 1, which induces the scattering rate given by

$$\begin{aligned}\tau_{n\mathbf{k}}^{-1} = & \frac{2\pi}{\hbar}\sum_{m\nu}\int\frac{d^2\mathbf{q}}{\Omega^{BZ}}|g_{mn\nu}(\mathbf{k},\mathbf{q})|^2 \\ & \times\Big[(n_{\mathbf{q}\nu}+1-f^0_{m\mathbf{k}+\mathbf{q}})\delta(\varepsilon_{n\mathbf{k}}-\varepsilon_{m\mathbf{k}+\mathbf{q}}-\hbar\omega_{\mathbf{q}\nu}) \\ & +(n_{\mathbf{q}\nu}+f^0_{m\mathbf{k}+\mathbf{q}})\delta(\varepsilon_{n\mathbf{k}}-\varepsilon_{m\mathbf{k}+\mathbf{q}}+\hbar\omega_{\mathbf{q}\nu})\Big],\end{aligned} \tag{2}$$

where $g_{mn\nu}(\mathbf{k}, \mathbf{q})$ is the electron-phonon matrix element with phonon frequency $\omega_{\mathbf{q}\nu}$, $\varepsilon_{n\mathbf{k}}$ and $\varepsilon_{m\mathbf{k}+\mathbf{q}}$ are eigenvalues, $f_{n\mathbf{k}}$ is the Fermi-Dirac distribution, $n_{\mathbf{q}\nu}$ is the Bose–Einstein distribution. The drift mobility μ is given by

$$\mu_{\alpha\beta} = \sigma_{\alpha\beta}/(en^c) \tag{3}$$

where we use a carrier concentration of $n^c = 10^{10}$ cm^{-2} which is the intrinsic regime where μ is independent of n^c. Due to crystal symmetry, $\mu = \mu_{xx} = \mu_{yy}$, $\sigma = \sigma_{xx} = \sigma_{yy}$ in all the III-V monolayers. More details about mobility calculations are given in a related work[33]. Here, we focus on the conductivity of doped systems. When a heavy doping such as $n^c = 10^{13}$ cm^{-2} is applied, the EPI would be significantly modified compared with the pristine regime. Thus, in the heavy doping cases, structural optimizations, electron and phonon dispersions, as well as conductivities are calculated independently. In the following, σ_c is used to denote the charge conductivity.

Figure 1 presents the room temperature mobilities of the pristine monolayers and the conductivities of doped systems. All the materials exhibit high electron mobilities, thanks to the small electron-effective mass and the single valley in the conduction bands. More variations in the hole mobility are observed due to the multi-peak band structures. The two arsenides present different mobilities of 14 and 289 cm^2/Vs, while two similar values, 940 and 904, are observed in the antimonides. A detailed analysis of mobility mechanisms is given in another work[33]. In this paper, the conductivities in doped III-V monolayers are extensively explained.

Doping is a practical method to tune the transport properties of semiconductors[34]. Sufficient carriers are induced by heavy doping, which turns semiconductors into metallic systems where SHE can occur. Considering the densities of states (DOS), an electron doping of 1×10^{13} cm^{-2} and a hole doping of 2×10^{13} cm^{-2} are respectively applied to the III-V monolayers, whose structures have been relaxed again. The main impact of such doping is the shift of Fermi energy (E_F) by a few hundred meV, leaving the crystal structure and electronic bands nearly unaffected as verified by Supplementary Fig. 3. Interestingly, an electron-hole asymmetry occurs in the phonon dispersions of the III-V monolayers: the phonon dispersion is weakly affected by electron doping, while the softening of longitudinal optical (LO) modes specifically occurs in the hole doping cases as shown in Fig. 2. The asymmetry can be explained by the difference in conduction and valence bands. For electron doping, the Γ valley is mainly occupied, leading to a limited change compared with the conduction bands in the pristine case. In contrast, for hole doping, multiple inequivalent peaks around Γ and K points enter into the transport window, enhancing the effective scattering $\frac{-\partial f^0_{n\mathbf{k}}}{\partial\varepsilon_{n\mathbf{k}}}\tau^{-1}_{n\mathbf{k}}$. Besides, attributed to the higher carrier concentration of 2×10^{13} cm^{-2} and consequent stronger screening effect, the hole doping induces a stronger phonon softening effect, which also occurs in other hole-doped III-V monolayers, see details in Supplementary Fig. 4. In a nutshell, the asymmetry in the conduction and valence bands leads to a limited scattering in electron-doped systems as verified by the high σ_c^e in Fig. 1a and an enhanced scattering in hole-doped systems as verified by the low σ_c^h in Fig. 1b.

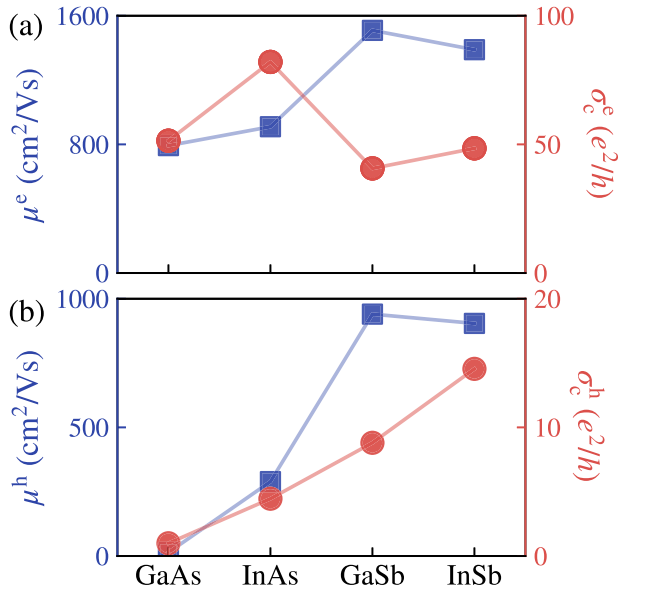

Fig. 1 | Charge transport properties of III-V monolayers. Drift mobilities of pristine semiconductors and charge conductivities of doped systems at 300 K are respectively represented by the blue square and red dot markers. μ^e and μ^h denote **a** electron and **b** hole mobilities of pristine semiconductors with square markers (left axis), σ_c^e and σ_c^h indicate the charge conductivities of **a** 1×10^{13} cm^{-2} electron-doped and **b** 2×10^{13}cm^{-2} hole-doped systems with circle markers (right axis).

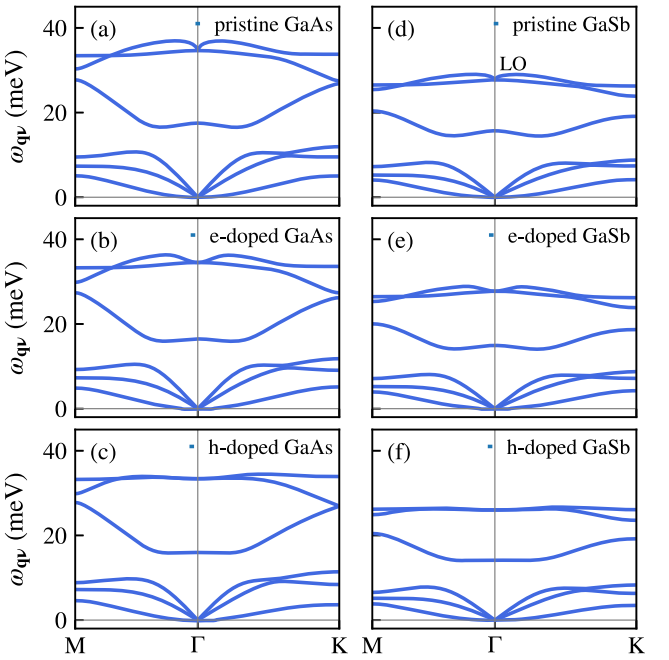

Fig. 2 | Phonon dispersions. For GaAs monolayer (**a**–**c**) and for GaSb monolayer (**d**–**f**). The first, second, and third rows show the results of pristine semiconductors, 1×10^{13} cm^{-2} electron-doped systems, and 2×10^{13} cm^{-2} hole-doped systems, respectively.

It is expected that the charge conductivity should be proportional to the carrier mobility. However, Fig. 1a illustrates that GaAs present a much lower μ^e but higher σ_c^e than GaSb with the same electron doping. In Fig. 1b, GaSb shows a high μ^h but a low σ_c^h with the hole doping. These unusual behaviors are attributed to the heavy doping, which leads to a distinct transport from the intrinsic case. In intrinsic semiconductors, the mobility is independent

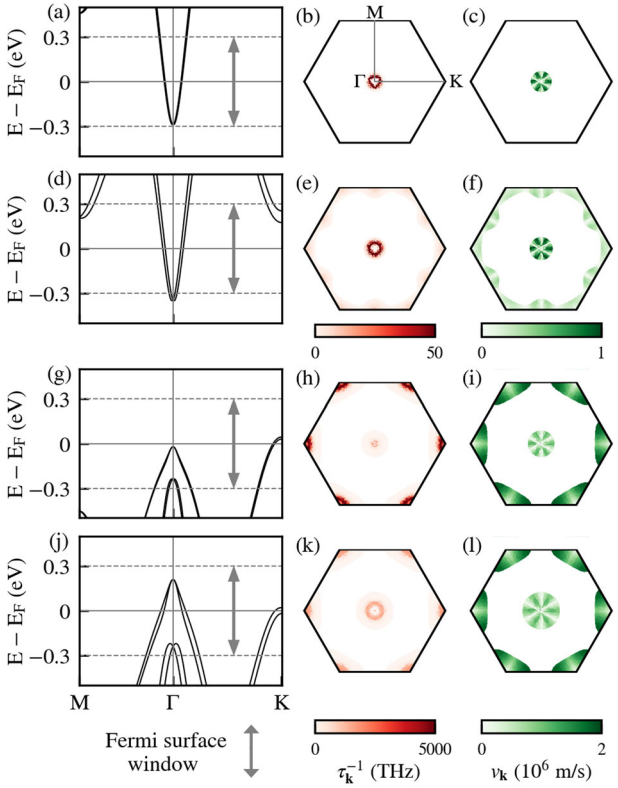

Fig. 3 | Scattering diagnosis. Electronic structures, **k**-resolved scattering rates, and **k**-resolved velocities for charge conductivities of **a**–**c** electron-doped GaAs, **d**–**f** electron-doped GaSb, **g**–**i** hole-doped GaAs, and **j**–**l** hole-doped GaSb. The vertical arrow denotes a Fermi surface window of 0.3 eV around E_F.

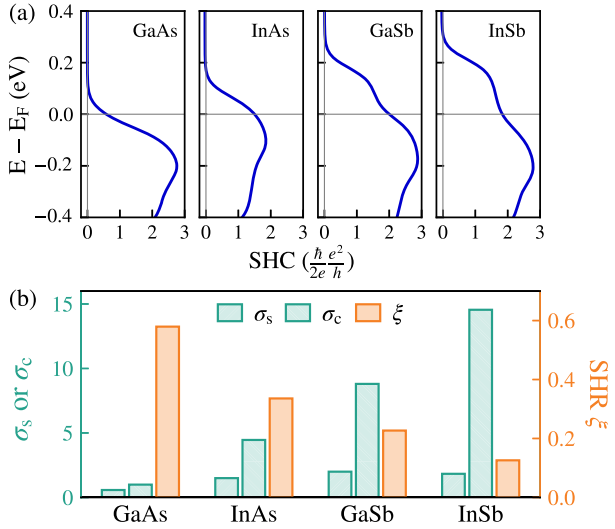

Fig. 4 | Results of spin Hall conductivities and ratios. All the systems are doped by a 2×10^{13} cm^{-2} hole carrier concentration. **a** Energy-dependent spin Hall conductivities at 300 K. **b** Spin Hall conductivities σ_s at E_F (unit: $(\hbar/2e)e^2/h$), charge conductivities σ_c (unit: e^2/h), and spin Hall ratios ξ.

of n^c. However, in heavy doping cases, semiconductors acquire a metallic character, and the mobility in doped systems depends on the band structure as well as E_F location determined by doping concentration. As a result, the linearly proportional relation between undoped mobility and heavily doped conductivity is no longer valid. The effect on transport induced by doping will be interpreted within the self-energy relaxation time approximation[32], where the conductivity is inversely proportional to the scattering rate and directly proportional to carrier velocity. Considering the Fermi-Dirac distribution at equilibrium and 300 K, we define the **k**-resolved scattering rates as $\tau_{\mathbf{k}}^{-1} = \sum_n \frac{-\partial f^0_{n\mathbf{k}}}{\partial \varepsilon_{n\mathbf{k}}} \tau_{n\mathbf{k}}^{-1}$, and **k**-resolved velocities as $v_{\mathbf{k}} = \sum_n v_{n\mathbf{k}}$, where n denotes the number of bands involved in the transport. Figure 3 compares the electronic structures, $\tau_{\mathbf{k}}^{-1}$, and $v_{\mathbf{k}}$ of doped GaAs and GaSb. The broken-inversion symmetry in pristine GaAs and GaSb monolayers results in a Rashba splitting[35] in the conduction band minimum (CBM) which can be regarded as a single valley. After electron doping, Fig. 3a shows that for GaAs, the single valley is preserved in the Fermi surface window [$E_F - 0.3$ eV, $E_F + 0.3$ eV], while Fig. 3d shows that for GaSb, more states around M and K points enter into the window, leading to enhanced scatterings with states that possess low velocities. As a result, σ_c^e in GaSb is reduced, as shown in Fig. 1a. The surprising behaviors of μ^h and σ_c^h of GaSb in Fig. 1b can be attributed to the doping-induced E_F shift. The valence band maximum (VBM) of pristine GaAs locates at K points, leading to a multi-peak band structure and a high DOS around VBM, thus the hole doping can only induce a small E_F shift, as shown in Fig. 3g. Besides, the spin-orbit splitting at K in the electronic band is 12 meV, which matches well with the phonon energy at K in the phonon dispersion [see Fig. 2c]. Considering momentum and energy conservations, the strong inter-peak scatterings between the K and K' peaks are allowed in hole-doped GaAs. Differently, the VBM in pristine GaSb is located at Γ, which is a single peak for the hole mobility and leads to a high μ^h. The single-peak band structure gives a small DOS around VBM, thus a large E_F shift of 0.21 eV is induced by the hole doping as shown in Fig. 3j, leading the states around K to dominate the scattering. Considering the low velocities at K points, σ_c^h is greatly reduced compared with μ^h in GaSb. It should be noted that for GaSb, the spin-orbit splitting at K is 40 meV, mismatching the phonon energy [see Fig. 2f], thus the inter-peak scattering between K and K' is weakened compared with GaAs, as shown by the colors in Fig. 3h and k. The discussions above demonstrate that doping is an effective way to manipulate the electronic structure, further controlling the EPI and charge conductivity in semiconductors. Analyses of scatterings in other III-V monolayers are similar, as given in Supplementary Fig. 5.

Spin Hall conductivity

SHE is composed of intrinsic and extrinsic contributions. The former is defined by the Kubo formula, and the latter is due to the skew-scattering and side-jump mechanisms, strongly dependent on disorder[36–38]. In this work, we focus on the intrinsic SHC in a weak scattering limit. With spin current along x, electric field along y, and spin orientation along z direction, the intrinsic SHC is calculated using Kubo formula[39,40]:

$$\sigma_s = \frac{\hbar}{2e}\frac{e^2}{\hbar}\int_{BZ}\frac{d^2\mathbf{k}}{(2\pi)^2}\Omega_s(\mathbf{k}), \tag{4}$$

where $\Omega_s(\mathbf{k}) = \sum_n f_{n\mathbf{k}}\Omega_{s,n}(\mathbf{k})$ is the spin Berry curvature (SBC) with $f_{n\mathbf{k}}$ at 300 K and the band-resolved SBC as

$$\Omega_{s,n}(\mathbf{k}) = \hbar^2 \sum_{m\neq n} \frac{-2\,\mathrm{Im}[\langle n\mathbf{k}|\hat{j}_z|m\mathbf{k}\rangle\langle m\mathbf{k}|\hat{v}_y|n\mathbf{k}\rangle]}{(\varepsilon_{n\mathbf{k}} - \varepsilon_{m\mathbf{k}})^2 + \eta^2}, \tag{5}$$

where $\hat{j}_z = \frac{1}{2}\{\hat{\sigma}_z\hat{v}_x + \hat{v}_x\hat{\sigma}_z\}$ is the spin current operator, $\hat{\sigma}_z$ is the Pauli operator, $\hat{v}_x$ and $\hat{v}_y$ are velocity operators. Considering the SOC strength in all the materials, a broadening of $\eta = 2$ meV is used as a weak scattering induced by extrinsic factors[41], and the η value has been validated in Supplementary Fig. 6. Due to the low conductivities, the hole-doped systems are more promising for high SHRs, thus III-V monolayer with 2×10^{13} cm^{-2} hole doping are targeted for SHCs, and this doping level has been realized in 2D systems[42,43].

Figure 4a presents the energy-dependent SHCs of hole-doped materials at room temperature. GaAs exhibits $\sigma_s^h = 0.6$ $(\hbar/2e)e^2/h$ due to the small E_F shift induced by doping. More prominently, SHCs of InAs, GaSb, and InSb can reach up to 1.5, 2.0, and 1.8 $(\hbar/2e)e^2/h$, respectively. For

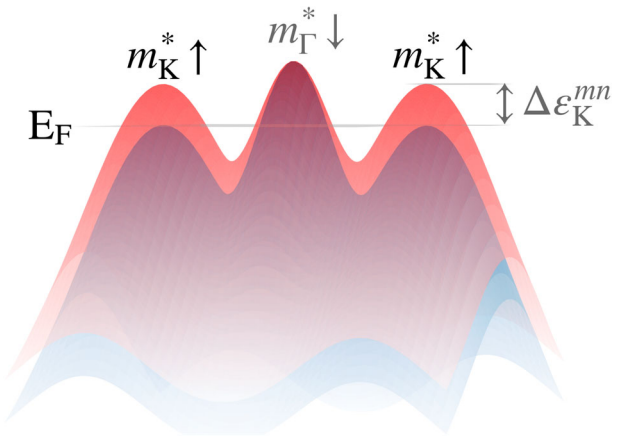

Fig. 5 | Diagram of the ideal band structure for high spin Hall ratio. The red and blue dispersions denote the bands projected by positive and negative spin Berry curvatures, respectively. The band structure shows multiple **k**-inequivalent extrema which present large effective mass m_K^*, and Fermi energy E_F inside the spin-orbit splitting $\Delta\varepsilon_K^{mn}$. In addition, small m_Γ^* can facilitate the E_F shift by doping if $\varepsilon_\Gamma > \varepsilon_K$.

comparison, MoS_2 monolayer only reaches $\sigma_s^h \approx 0.2\,(\hbar/2e)e^2/h$ [22]. The high SHCs in hole-doped III-V monolayers are attributed to the in-gap E_F location, as shown in Fig. 3j. The spin-orbit gap separates the positive and negative SBC. When the E_F locates inside the spin-orbit gap, SHC, as the integration over the Fermi sea of SBC, can be maximized by the sign-invariant SBC over all the **k**-points. The SBC decompositions of all the materials are presented in Supplementary Fig. 8. For GaAs, the SBC originates from both K and Γ points, while for the others, the SBC mainly stems from the Γ point due to the in-gap E_F at Γ. The discussions above highlight that the doping in semiconductors can yield large SHCs in III-V monolayers.

Spin Hall ratio

With the charge conductivities σ_c and spin Hall conductivities σ_s, the spin Hall ratio $\xi = \frac{2e}{\hbar}|\frac{\sigma_s}{\sigma_c}|$ can be discussed in hole-doped systems. It has been illustrated in Supplementary Table 1 that the computational and experimental SHR values coincide with each other, i.e., both present $\xi \sim 0.01$ in heavy metals, demonstrating the effectiveness of our calculations. Figure 4b shows that large σ_s^h values are found in antimonides which also possess fairly large σ_c^h, as a result, GaSb and InSb exhibit $\xi^h = 0.23$ and 0.13, respectively. More importantly, hole-doped arsenides are perfect candidates with high SHCs and low charge transports, yielding exceptional $\xi^h = 0.58$ and 0.34 in GaAs and InAs, respectively. Compared with heavy metals where $\xi \sim 0.01$, the hole-doped GaAs and other III-V monolayers exhibit great potential for efficient charge-to-spin conversion.

Spin Hall ratio descriptor

Taking the transport behaviors in III-V monolayers as a prototype, a descriptor to enhance SHR can be proposed. The idea is to decrease the charge conductivity as well as increase SHC. Large effective mass reduces σ_c via lowering down the carrier velocity. As shown in Fig. 3, the band structure with multiple extrema around E_F can enhance scattering. Besides, the energy-dependent SHCs demonstrate that SHC can be maximized by locating E_F in the spin-orbit gap. Overall, a band structure descriptor for high SHR can be proposed as depicted in Fig. 5: (1) large effective mass m_K^* around E_F; (2) multiple **k**-inequivalent extrema around E_F; (3) a E_F located inside the spin-orbit splitting $\Delta\varepsilon_K^{mn}$. It should be stressed that within a limited doping concentration, there is a competition between the first two conditions and the last one, since flat and multiple band extrema would induce a large DOS, which hinders the tuning of E_F. A small effective mass at Γ point, m_Γ^*, is also preferred for tuning E_F when $\varepsilon_\Gamma > \varepsilon_K$. In short, a delicate balance between σ_c and σ_s is essential for SHR enhancement.

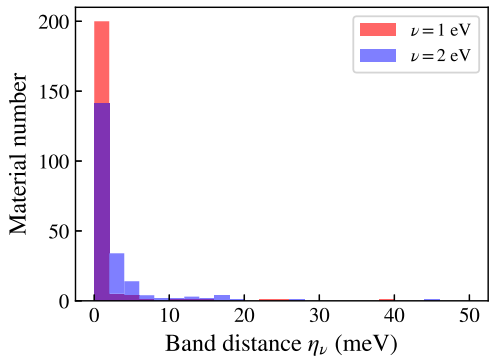

Fig. 6 | Band distances of 216 monolayer semiconductors. Denoted by η_ν given by Eq. (6), the band distance indicates the discrepancy between DFT and Wannier results in the bands below CBM+ν in energy.

High-throughput calculations

Potential candidates for high SHR can be found by screening a database with the aforementioned descriptor. Focusing on the 2D materials, we perform fully relativistic high-throughput calculations for exfoliable monolayers. From the MC2D database[44,45], all the rare-earth free materials with up to 6 atoms per unit cell are considered, yielding 216 semiconductors which are employed for the fully relativistic DFT calculations and Wannierizations. The band interpolation quality of Wannier Hamiltonian is measured by the average band distance, given as[46,47]

$$\eta_\nu = \sqrt{\frac{\sum_{n\mathbf{k}} \tilde{f}_{n\mathbf{k}} \left(\varepsilon_{n\mathbf{k}}^{\mathrm{DFT}} - \varepsilon_{n\mathbf{k}}^{\mathrm{Wan}}\right)^2}{\sum_{n\mathbf{k}} \tilde{f}_{n\mathbf{k}}}} \tag{6}$$

where **k** is the eigenstate along the high-symmetry **k**-path for band structure, $\tilde{f}_{n\mathbf{k}} = \sqrt{f_{n\mathbf{k}}^{\mathrm{DFT}}(E_F+\nu,\sigma) f_{n\mathbf{k}}^{\mathrm{Wan}}(E_F+\nu,\sigma)}$ where $f(E_F+\nu,\sigma)$ is the Fermi-Dirac distribution. Here $E_F+\nu$ and σ respectively represent energy position and smearing value for the distribution, thus we can focus on the bands below $E_F+\nu$ in energy. E_F is set as the CBM of semiconductor, and σ is fixed to be 300 K. Since the Wannier Hamiltonian describes the low-energy valence electrons, it is expected that the Wannier-interpolated band will deviate more from the DFT results in the higher conduction band region. Therefore, the higher ν is, the larger η_ν is expected to be. The symbols η_1 and η_2 denote the band distance for the bands below E_F+1 eV and E_F+2 eV, respectively, and the band distances of 216 materials are present in Fig. 6. For the bands below E_F+1 eV, 97% (210/216) of materials show a small band distance below 10 meV, and 93% (200/216) of materials show a very small band distance below 2 meV. For the bands below E_F+2 eV, 90% (195/216) of materials show a distance below 10 meV, and 65% (141/216) of materials show a distance below 2 meV, highlighting the overall quality of Wannier Hamiltonians in our database.

Figure 7 shows the electron and hole effective masses of all the semiconductors, as well as SHC values in the doped systems where a doping concentration of 2×10^{13} cm^{-2} is employed for both carriers. The effective mass is calculated by $m_{\alpha\alpha}^* = (\frac{1}{\hbar^2}\frac{d^2\varepsilon}{dk_\alpha^2})^{-1}$ ($\alpha = x, y$) through the interpolation around CBM and VBM, respectively, for electron and hole. Overall, the hole presents a larger effective mass than the electron, and hole-doped materials exhibit larger SHC values. Nevertheless, many materials with high SHCs present small effective masses, populated at the left lower corner in Fig. 7b. Still, by setting the screening conditions as $m_{xx}^* \approx m_{yy}^* > 0.5\,m_0$, multiple band extrema around E_F, and SHC >0.4 $(\hbar/2e)e^2/h$, two MXene monolayers are selected as candidates, Sc_2CCl_2 and Y_2CBr_2. All the effective masses, doped SHCs, energy gaps, and band structures of all the 216 semiconductors are reported in Supplementary Table 5 and its followings.

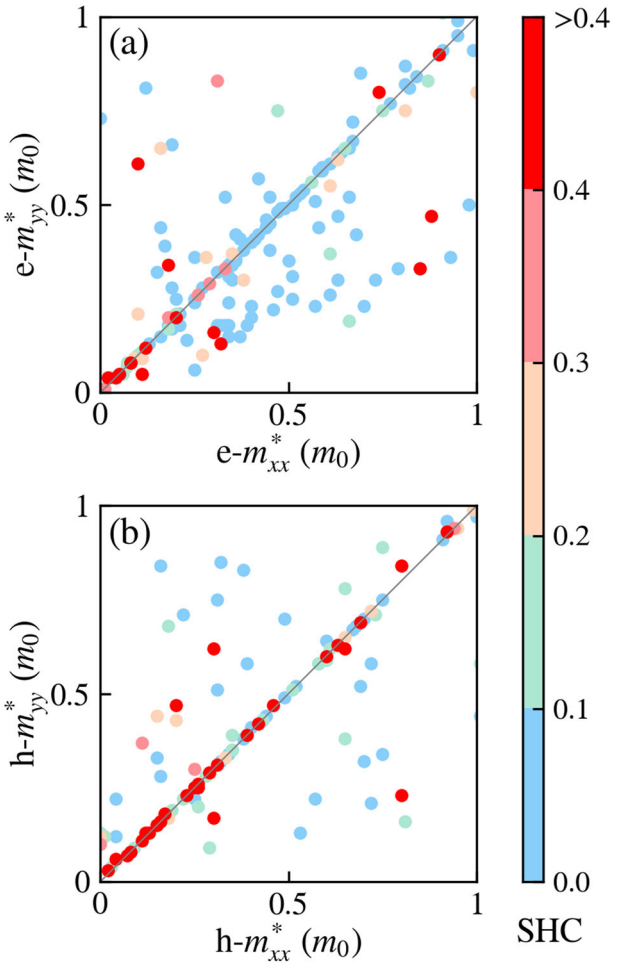

Fig. 7 | Effective masses of 216 monolayer semiconductors. a Electron and **b** hole effective masses along *x* and *y* directions. Spin Hall conductivities (unit: $(\hbar/2e)e^2/h$) are given by the colorbar in electron- and hole-doped systems, respectively. Diagonal lines denote isotropic materials where $m^*_{xx} = m^*_{yy}$.

Results of MXene monolayers

Sc_2CCl_2 and Y_2CBr_2 present similarities since they are composed of homologous elements. After a full relaxation considering the hole doping, both structures present a P-3m1 space group, as shown in Fig. 8d. Figure 8a and e illustrate the hole-doped band structures of Sc_2CCl_2 and Y_2CBr_2, respectively. The SOC splitting induces two peaks around Γ point, and the top band presents an effective mass $m^*_{xx} = m^*_{yy} \approx 0.7\, m_0$. E_F locates inside the gap, leading to high $\sigma^h_s = 0.5\ (\hbar/2e)e^2/h$. It has been verified that SHCs in both materials are robust against broadening, and the main SBC contributions originate from the Γ point, details are given in Supplementary Fig. 12. Compared with Y_2CBr_2 possessing an SOC gap of 75 meV at Γ, Sc_2CCl_2 shows a smaller gap of 20 meV due to lighter elements. Apart from the Γ point, eigenstates around the M point also enter into the Fermi surface window. Figure 8b, f validate the mechanical stabilities of hole-doped Sc_2CCl_2 and Y_2CBr_2 monolayers by showing phonon dispersions without imaginary frequency. Phonon dispersions illustrate that Sc_2CCl_2 presents higher-energy modes than Y_2CBr_2. Figure 8c and g show the **k**-resolved scattering rates of both materials. Sc_2CCl_2 exhibits dominant scattering as high as 836 THz around the Γ point. This high rate is attributed to its small SOC gap of 20 meV which matches the phonon energy $\omega_{n\Gamma}$. On the other hand, the scattering in Y_2CBr_2 is limited to 370 THz, since its large gap of 75 meV goes beyond its phonon energy range. Compared with the Γ point, scatterings around M points are quite weak. This is attributed to $\varepsilon_M = -273$ meV for Sc_2CCl_2 and −57 meV for Y_2CBr_2, thus the scattering contributions are greatly limited by the large distance from E_F. Overall, Sc_2CCl_2 presents lower $\sigma^h_c = 2.2\ e^2/h$ while Y_2CBr_2 shows $\sigma^h_c = 3.9\ e^2/h$ in Fig. 8h. Benefiting from the low charge conductivity, the SHR in Sc_2CCl_2 is computed to be $\xi^h = 0.22$, and Y_2CBr_2 possesses $\xi^h = 0.12$. The discovery of an MXene monolayer with high SHR validates the effectiveness of the SHR descriptor.

Discussions of III-V monolayers and MXene monolayers indicate that compared with the materials composed of heavy elements, the light materials can be more promising for high SHR. Although the heavy elements induce strong SOC for SHC enhancement, they also result in large band splitting and low-energy phonon mode simultaneously. By breaking the energy conservation rule, these two factors reduce the electron-phonon coupling and hinder the scatterings in charge transport. As a result, the charge conductivity is also enhanced. Since the charge-to-spin conversion is an interrelated process, balancing charge and spin transports is critical to

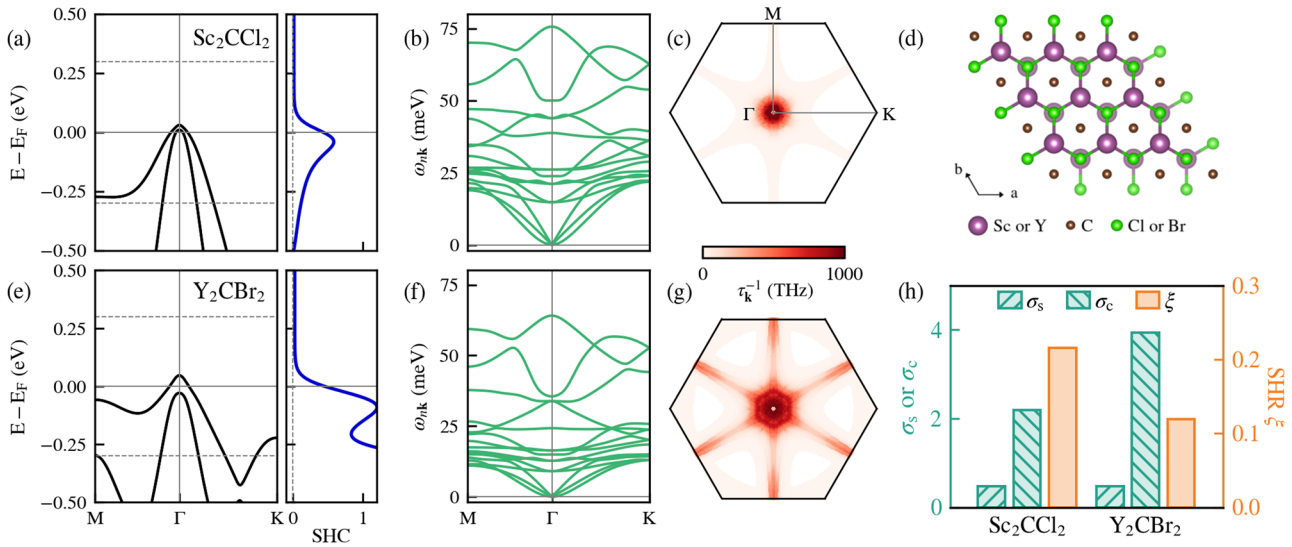

Fig. 8 | Hole-doped Sc_2CCl_2 and Y_2CBr_2 monolayers results. a–**c** and **e**–**g** denote electronic structures, energy-dependent spin Hall conductivities in units of $(\hbar/2e)e^2/h$, phonon dispersions, and scattering rates $\tau^{-1}_{\mathbf{k}}$ of Sc_2CCl_2 and Y_2CBr_2, respectively. **d** presents the atomic structure, and **h** shows spin Hall conductivities (unit: $(\hbar/2e)e^2/h$), charge conductivities (unit: e^2/h), and spin Hall ratios of both materials.

enhance SHR rather than only maximize SHC. In addition, compared with the SHR $\xi^h = 0.58$ in GaAs, $\xi^h = 0.22$ in Sc_2CCl_2 is relatively lower. Considering that the SHC values in the two materials are similar, the SHR difference is attributed to the high σ_c^h in Sc_2CCl_2. In GaAs, strong inter-peak scatterings occur [see Fig. 3h] thanks to the K eigenstates around E_F. In contrast, Sc_2CCl_2 exhibits weak scatterings around the M point [see Fig. 8c] due to the M eigenstates far away from E_F. Besides, the inversion symmetry keeps the band degeneracy in Sc_2CCl_2, further reducing the scattering possibilities. This comparison demonstrates the importance of multi-peaks around E_F to reduce charge conductivity, further validating the SHR descriptor. By expanding the high-throughput calculations database, materials with more ideal electronic structures and phonon frequencies could be found for SHR enhancement.

Experimental feasibility

Charge-to-spin conversion has been realized in MoS_2 and WSe_2 monolayers grown by chemical vapor deposition[19]. Since the first synthesis of 2D AlN layers by metal organic deposition[48], many efforts have been devoted to the synthesis of other 2D III-V materials[49,50]. For example, GaSb films can be grown via a seeded lateral epitaxy, and the free-standing crystalline GaSb can be exfoliated from these films[51]. Moreover, 2D InAs flakes with high crystalline quality have been synthesized through van der Waals epitaxy with a thickness down to 4.8 nm[52]. Due to chemical similarity in one family, we expect similar techniques can be applied to the other III-V monolayers. Two promising materials, Sc_2CCl_2 and Y_2CBr_2, are easily exfoliable from their van der Waals bulk compounds[45]. Finally, the doping levels proposed in this work can be realized via the advanced technique of electron beam, which implements the doping of 1.7×10^{13} cm^{-2} in 2D systems[42]. The doped state persists even after removing the electron beam and back-gate voltage, and the process is reversible and repeatable[42]. Moreover, the doping level over 5×10^{13} cm^{-2} has been realized in MoS_2 monolayers via the ionic-liquid gate[43].

In conclusion, 2D materials with high spin Hall ratios have been found using a multidisciplinary investigation involving charge transport, spin Hall conductivity, and a high-throughput database. The hole-doped GaAs monolayer presents an ultrahigh SHR of $\xi = 0.58$, attributed to the strong scattering and the high SHC. An SHR descriptor is proposed and validated by a high-throughput database of 216 exfoliable monolayer semiconductors, suggesting a new promising material, Sc_2CCl_2. Besides, this database is fully released to the community. This work reveals potential 2D materials for efficient charge-to-spin conversion, providing a guideline for materials discovery in spintronics.

Methods

DFT calculations

DFT and DFPT calculations are performed by the QUANTUM ESPRESSO package[53]. The fully relativistic norm-conserving pseudopotentials PseudoDojo[54] within the Perdew–Burke–Ernzerhof (PBE) parametrization of the generalized gradient approximation (GGA)[54]. The cutoff energy for wavefunctions is set to 120 Ry. We use a 2D Coulomb truncation[55]. Fully relativistic computations have been performed for structural relaxation, self-consistent, non-self-consistent, and phonon calculations. Relaxations are performed respectively for pristine and doped materials. Variable cell relaxation is performed with total energy convergence of 10^{-8} Ry, force convergence of 10^{-4} Ry/Bohr, and pressure convergence of 0.1 kbar.

Charge conductivity calculations

The drift mobility and charge conductivity are calculated using the EPW package[56,57], where the electron-phonon coupling is interpolated from coarse $\mathbf{k}/\mathbf{q}$-grids to fine $\mathbf{k}/\mathbf{q}$-grids using Wannier functions with the considerations of dipole, quadrupole, and gauge-covariant contributions[58,59]. A coarse $12 \times 12 \times 1$ $\mathbf{k}/\mathbf{q}$-grid is adopted in ab initio calculations, then a fine $\mathbf{k}/\mathbf{q}$-grid of $720 \times 720 \times 1$ is used for electron mobility, and $\mathbf{k}/\mathbf{q}$-grid of $360 \times 360 \times 1$ for hole mobility and charge conductivity of doped systems. Note that in the calculation at the zone-center $\mathbf{q} = \Gamma$, a denser $\mathbf{k}$-grid of $32 \times 32 \times 1$ is used in DFPT calculation to get convergent electrostatic properties. A Fermi surface window of 0.3 eV has been validated for convergence and employed in all calculations. An adaptive smearing[60] is applied in the energy-conserving delta functions, and a phonon frequency cutoff of 1 cm^{-1} is employed. The calculations are performed at room temperature.

Spin Hall conductivity calculations

The spin Hall conductivity is calculated by Wannier90 package[39,61], with a $12 \times 12 \times 1$ coarse $\mathbf{k}$-grid in ab initio calculation, and a fine $\mathbf{k}$-grid of $360 \times 360 \times 1$ for the Wannier interpolation. A Fermi-Dirac distribution function of 300 K and a broadening of 2 meV have been considered.

High-throughput calculations

The fully relativistic DFT calculations and Wannierizations have been performed using AiiDA[62] and PseudoDojo[54] on 216 materials from the MC2D database[44,45]. The initial guess for projectors is given by the orbital information in PseudoDojo[63]. The semicore orbitals corresponding to deep bands are excluded from projections. A small trial step is used in the minimization of the spread function to stabilize the Wannierization, and a large number of iterations is used to converge. The maximum of the frozen window is set as CBM + 2 eV, which is verified to be the optimal value by Supplementary Fig. 13. The script for the automated generation of the Wannier90 input file is provided[64]. To provide a high-quality Wannier Hamiltonian database, failed cases (23/216) have been manually corrected by tuning the frozen window, increasing the number of Bloch wavefunctions, or manually modifying initial projections.

Data availability

For the III-V and MXene monolayers investigated in this work, details of the relaxed atomic structures, effective masses, densities of states, doping levels, and electron and phonon dispersions are given in Supplementary Material, and input and output files for computations are given on Materials Cloud Archive[64]. The input and output files, pseudopotentials, as well as Wannier Hamiltonians and band structures of 216 monolayer semiconductors, are provided on Materials Cloud Archive[64].

Received: 20 June 2024; Accepted: 6 October 2024;
Published online: 23 October 2024

References

1. Inoue, J. & Ohno, H. Taking the Hall effect for a spin. *Science* **309**, 2004 (2005).
2. Chang, C.-Z. & Li, M. Quantum anomalous Hall effect in time-reversal-symmetry breaking topological insulators. *J. Phys. Condens. Matter* **28**, 123002 (2016).
3. Ashcroft,N., W. & Mermin, N. D. *Solid State Physics* (Hartcourt College publisher, 1976)
4. Sinova, J., Valenzuela, S. O., Wunderlich, J., Back, C. H. & Jungwirth, T. Spin Hall effects. *Rev. Mod. Phys.* **87**, 1213 (2015).
5. Manchon, A. et al. Current-induced spin-orbit torques in ferromagnetic and antiferromagnetic systems. *Rev. Mod. Phys.* **91**, 035004 (2019).
6. Guo, Z. et al. Spintronics for energy- efficient computing: an overview and outlook. *Proc. IEEE* **109**, 1398 (2021).
7. Žutić, I., Fabian, J. & Das Sarma, S. Spintronics: fundamentals and applications. *Rev. Mod. Phys.* **76**, 323 (2004).
8. Olejník, K. et al. Detection of electrically modulated inverse spin hall effect in an Fe/GaAs microdevice. *Phys. Rev. Lett.* **109**, 076601 (2012).
9. Tao, X. et al. Self-consistent determination of spin Hall angle and spin diffusion length in Pt and Pd: the role of the interface spin loss. *Sci. Adv.* **4**, eaat1670 (2018).
10. Dc, M. et al. Room-temperature high spin-orbit torque due to quantum confinement in sputtered Bi_xSe_{1-x} films. *Nat. Mater.* **17**, 800 (2018).
11. Khang, N. H. D., Ueda, Y. & Hai, P. N. A conductive topological insulator with large spin Hall effect for ultralow power spin-orbit torque switching. *Nat. Mater.* **17**, 808 (2018).

12. Zhou, J., Qiao, J., Bournel, A. & Zhao, W. Intrinsic spin Hall conductivity of the semimetals $MoTe_2$ and WTe_2. *Phys. Rev. B* **99**, 060408(R) (2019).
13. Zhao, B. et al. Observation of charge to spin conversion in Weyl semimetal WTe_2 at room temperature. *Phys. Rev. Res.* **2**, 013286 (2020).
14. Vila, M. et al. Low-symmetry topological materials for large charge-to-spin interconversion: the case of transition metal dichalcogenide monolayers. *Phys. Rev. Res.* **3**, 043230 (2021).
15. Song, P. et al. Coexistence of large conventional and planar spin Hall effect with long spin diffusion length in a low-symmetry semimetal at room temperature. *Nat. Mater.* **19**, 292 (2020).
16. Marrazzo, A., Gibertini, M., Campi, D., Mounet, N. & Marzari, N. Relative abundance of Z_2 topological order in exfoliable two-dimensional insulators. *Nano Lett.* **19**, 8431 (2019).
17. Grassano, D., Marzari, N. & Campi, D. High-throughput screening of Weyl semimetals. *Phys. Rev. Mater.* **8**, 024201 (2024).
18. Dorow, C. et al. Advancing monolayer 2-d nmos and pmos transistor integration from growth to van der waals interface engineering for ultimate cmos scaling. *IEEE Trans. Electron Dev.* **68**, 6592 (2021).
19. Shao, Q. et al. Strong Rashba-Edelstein effect-induced spin-orbit torques in monolayer transition metal dichalcogenide/ferromagnet bilayers. *Nano Lett.* **16**, 7514 (2016).
20. Wang, H. et al. Interfacial engineering of ferromagnetism in wafer-scale van der Waals Fe_4GeTe_2 far above room temperature. *Nat. Commun.* **14**, 1 (2023).
21. Wang, H. et al. Room temperature energy-efficient spin-orbit torque switching in two-dimensional van der Waals Fe_3GeTe_2 induced by topological insulators. *Nat. Commun.* **14**, 1 (2023).
22. Feng, W. et al. Intrinsic spin Hall effect in monolayers of group-VI dichalcogenides: a first-principles study. *Phys. Rev. B* **86**, 165108 (2012).
23. Sohier, T., Campi, D., Marzari, N. & Gibertini, M. Mobility of two-dimensional materials from first principles in an accurate and automated framework. *Phys. Rev. Mater.* **2**, 114010 (2018).
24. Wang, H. et al. Spin Hall effect in prototype Rashba ferroelectrics GeTe and SnTe. *npj Comput. Mater.* **6**, 1 (2020).
25. Backman, J., Lee, Y. & Luisier, M. Electron-phonon calculations using a Wannier-based supercell approach: applications to the monolayer MoS_2 mobility. *Solid State Electron.* **198**, 108461 (2022).
26. Zhang, C., Wang, R., Mishra, H. & Liu, Y. Two-dimensional semiconductors with high intrinsic carrier mobility at room temperature. *Phys. Rev. Lett.* **130**, 087001 (2023).
27. Cepellotti, A., Coulter, J., Johansson, A., Fedorova, N. S. & Kozinsky, B. Phoebe: a high-performance framework for solving phonon and electron Boltzmann transport equations. *J. Phys. Mater.* **5**, 035003 (2022).
28. Giustino, F. Electron-phonon interactions from first principles. *Rev. Mod. Phys.* **89**, 015003 (2017).
29. Kohn, W. Nobel lecture: electronic structure of matter—wave functions and density functionals. *Rev. Mod. Phys.* **71**, 1253 (1999).
30. Baroni, S., de Gironcoli, S., Dal Corso, A. & Giannozzi, P. Phonons and related crystal properties from density-functional perturbation theory. *Rev. Mod. Phys.* **73**, 515 (2001).
31. Marzari, N., Mostofi, A. A., Yates, J. R., Souza, I. & Vanderbilt, D. Maximally localized Wannier functions: theory and applications. *Rev. Mod. Phys.* **84**, 1419 (2012).
32. Poncé, S., Li, W., Reichardt, S. & Giustino, F. First-principles calculations of charge carrier mobility and conductivity in bulk semiconductors and two-dimensional materials. *Rep. Prog. Phys.* **83**, 036501 (2020).
33. Zhou, J., Poncé, S. & Charlier, J.-C. Guidelines for accurate and efficient calculations of mobilities in two-dimensional materials. *Phys. Rev. B* **110**, 125304 (2024).
34. Awate, S. S. et al. Impact of large gate voltages and ultrathin polymer electrolytes on carrier density in electric-double-layer-gated two-dimensional crystal transistors. *ACS Appl. Mater. Interfaces* **15**, 15785 (2023).
35. Wu, K. et al. Two-dimensional giant tunable Rashba semiconductors with two-atom-thick buckled honeycomb structure. *Nano Lett.* **21**, 740 (2021).
36. Lowitzer, S. et al. Extrinsic and intrinsic contributions to the spin Hall effect of alloys. *Phys. Rev. Lett.* **106**, 056601 (2011).
37. Gorini, C., Eckern, U. & Raimondi, R. Spin Hall effects due to phonon skew scattering. *Phys. Rev. Lett.* **115**, 076602 (2015).
38. Shashank, U. et al. Disentanglement of intrinsic and extrinsic side-jump scattering induced spin Hall effect in N-implanted Pt. *Phys. Rev. B* **107**, 064402 (2023).
39. Qiao, J., Zhou, J., Yuan, Z. & Zhao, W. Calculation of intrinsic spin Hall conductivity by Wannier interpolation. *Phys. Rev. B* **98**, 214402 (2018).
40. Zhang, Y. et al. Different types of spin currents in the comprehensive materials database of nonmagnetic spin Hall effect. *npj Comput. Mater.* **7**, 1 (2021).
41. Li, H. et al. Intraband and interband spin-orbit torques in noncentrosymmetric ferromagnets. *Phys. Rev. B* **91**, 134402 (2015).
42. Shi, W. et al. High-order fractal quantum oscillations in graphene/BN superlattices in the extreme doping limit. *Phys. Rev. Lett.* **130**, 186204 (2023).
43. Sohier, T. et al. Enhanced electron-phonon interaction in multivalley materials. *Phys. Rev. X* **9**, 031019 (2019).
44. Mounet, N. et al. Two-dimensional materials from high-throughput computational exfoliation of experimentally known compounds. *Nat. Nanotechnol.* **13**, 246 (2018).
45. Campi, D., Mounet, N., Gibertini, M., Pizzi, G. & Marzari, N. Expansion of the materials cloud 2D database. *ACS Nano* **17**, 11268 (2023).
46. Qiao, J., Pizzi, G. & Marzari, N. Automated mixing of maximally localized Wannier functions into target manifolds. *npj Comput. Mater.* **9**, 1 (2023).
47. Qiao, J., Pizzi, G. & Marzari, N. Projectability disentanglement for accurate and automated electronic-structure Hamiltonians. *npj Comput. Mater.* **9**, 1 (2023).
48. Wang, W. et al. 2D AlN layers sandwiched between graphene and Si substrates. *Adv. Mater.* **31**, 1803448 (2019).
49. Lu, F., Wang, H., Zeng, M. & Fu, L. Infinite possibilities of ultrathin III-V semiconductors: starting from synthesis. *iScience* **25**, 103835 (2022).
50. Nikolaevich Klochkov, A. et al. Growth by molecular beam epitaxy and characterization of n-InAs films on sapphire substrates. *Appl. Surf. Sci.* **619**, 156722 (2023).
51. Manzo, S. et al. Pinhole-seeded lateral epitaxy and exfoliation of GaSb films on graphene-terminated surfaces. *Nat. Commun.* **13**, 1 (2022).
52. Dai, J. et al. Controlled growth of two-dimensional InAs single crystals via van der Waals epitaxy. *Nano Res.* **15**, 9954 (2022).
53. Giannozzi, P. et al. Advanced capabilities for materials modelling with Quantum ESPRESSO. *J. Phys. Condens. Matter* **29**, 465901 (2017).
54. van Setten, M. J. et al. The PseudoDojo: training and grading a 85 element optimized norm-conserving pseudopotential table. *Comput. Phys. Commun.* **226**, 39 (2018).
55. Sohier, T., Calandra, M. & Mauri, F. Density functional perturbation theory for gated two-dimensional heterostructures: theoretical developments and application to flexural phonons in graphene. *Phys. Rev. B* **96**, 075448 (2017).
56. Poncé, S., Margine, E., Verdi, C. & Giustino, F. EPW: electron-phonon coupling, transport and superconducting properties using maximally localized wannier functions. *Comput. Phys. Commun.* **209**, 116 (2016).
57. Lee, H. et al. Electron–phonon physics from first principles using the EPW code. *npj Comput. Mater.* **9**, 1 (2023).
58. Poncé, S., Royo, M., Stengel, M., Marzari, N. & Gibertini, M. Long-range electrostatic contribution to electron-phonon couplings and mobilities of two-dimensional and bulk materials. *Phys. Rev. B* **107**, 155424 (2023).
59. Poncé, S., Royo, M., Gibertini, M., Marzari, N. & Stengel, M. Accurate prediction of Hall mobilities in two-dimensional materials through gauge-covariant quadrupolar contributions. *Phys. Rev. Lett.* **130**, 166301 (2023).

60. Poncé, S. et al. First-principles predictions of Hall and drift mobilities in semiconductors. *Phys. Rev. Res.* **3**, 043022 (2021).
61. Pizzi, G. et al. Wannier90 as a community code: new features and applications. *J. Phys. Condens. Matter* **32**, 165902 (2020).
62. Huber, S. P. et al. AiiDA 1.0, a scalable computational infrastructure for automated reproducible workflows and data provenance. *Sci. Data* **7**, 1 (2020).
63. Pseudodojo semicore states. https://github.com/aiidateam/aiida-wannier90-workflows/blob/main/src/aiida_wannier90_workflows/utils/pseudo/data/semicore/PseudoDojo_0.4_PBE_FR_standard_upf.json Github (2023).
64. Materials Cloud Archive. https://archive.materialscloud.org/deposit/records/2138 (2024).

Acknowledgements

The authors would like to thank Xi Dai, Matteo Giantomassi, and Junfeng Qiao for fruitful discussions. S.P. acknowledges the support from the Fonds de la Recherche Scientifique de Belgique (F.R.S.-FNRS). J.Z. and J.-C.C. acknowledge financial support from the Fédération Wallonie-Bruxelles through the ARC Grant "DREAMS" (No. 21/26-116), from the EOS project "CONNECT" (No. 40007563), and from the Belgium F.R.S.-FNRS through the research project (No. T.029.22F). Computational resources have been provided by the PRACE award granting access to MareNostrum4 at Barcelona Supercomputing Center (BSC), Spain and Discoverer in SofiaTech, Bulgaria (OptoSpin project ID. 2020225411), and by the Consortium des Équipements de Calcul Intensif (CÉCI), funded by the F.R.S.-FNRS under Grant No. 2.5020.11 and by the Walloon Region, as well as computational resources awarded on the Belgian share of the EuroHPC LUMI supercomputer.

Author contributions

J.Z. designed the study and performed calculations. S.P. and J.-C.C. supervised the project. All authors analyzed the results and contributed to writing the paper.

Competing interests

The authors declare no competing interests.

Additional information

Supplementary information The online version contains supplementary material available at https://doi.org/10.1038/s41524-024-01434-z.

Correspondence and requests for materials should be addressed to Jiaqi Zhou, Samuel Poncé or Jean-Christophe Charlier.